Chapter

Plasmonic Excitations in Carbon Nanotubes: PIC Simulations vs Hydrodynamic Model

Pablo Martín-Luna, Alexandre Bonatto, Cristian Bontoiu, Guoxing Xia and Javier Resta-López

Abstract

Charged particles traveling along a carbon nanotube (CNT) may produce the collective oscillation of the free electrons within the cylindrical graphene shell that makes up the nanotube wall. The associated electromagnetic modes (called plasmonic modes) are a potential candidate to achieve ultra-high accelerating gradients for particle acceleration. The plasmonic excitations can be studied by particle simulations and with analytical models. In this chapter, we firstly review different works that employ particle-in-cell (PIC) codes to simulate plasmonic excitations in carbon nanostructures. Then, the linearized hydrodynamic model is presented to analytically describe the plasmonic modes excited by a localized point-like charge propagating along a single-walled nanotube. In this model, the free electron gas at the nanotube wall is treated as a plasma, which satisfies the linearized continuity and momentum equations with specific solid-state properties. Finally, we compare the plasmonic excitations obtained using the hydrodynamic model with those from Fourier-Bessel PIC (FBPIC) simulations. A comprehensive analysis is conducted to examine similarities, differences, and limitations of both methods. This research offers an insightful viewpoint on the potential use of CNTs to enhance particle acceleration techniques, paving the way for future progress in high-energy physics and related fields.

Keywords: carbon nanotubes (CNTs), particle-in-cell (PIC) simulations, linearized hydrodynamic model, wakefield excitation, plasmonics, particle acceleration

1. Introduction

Particle accelerators play a crucial role in various domains, such as scientific research, industry, and national security. They have enabled cutting-edge research in high-energy physics for over half a century and are essential in synchrotron radiation and free electron lasers. Furthermore, they are widely used for medical applications, for example, in radiotherapy and hadrontherapy for cancer treatments. However, the conventional accelerators based on the radio frequency (RF) technology are limited to gradients in the order of 100 MV/m due to surface RF breakdown [1, 2]. For this reason, several alternative solutions are currently explored to overcome the

IntechOpen

limitation, such as dielectric laser or wakefield accelerators [3–6] and plasma-based accelerators [7–10].

In the 1980s and 1990s, Tajima *et al.* [11–13] proposed solid-state wakefield acceleration using the ion lattice of crystals as a potential technique to achieve acceleration gradients of several TV/m. In this technique, X-rays or charged particle bunches may be able to excite longitudinal wakefields while traveling along the crystal. However, the angstrom-sized channels in natural crystals impose limitations on beam intensity acceptance and dechanneling rates. These challenges need to be addressed to fully realize the potential of solid-state wakefield acceleration using crystals.

In this context, carbon nanotubes (CNTs) represent a potential candidate for obtaining ultra-high gradients. CNTs can display either metallic or semiconductor properties based on their rolling pattern and possess remarkable thermo-mechanical and electronic characteristics, along with dimensional flexibility. Since their discovery by Iijima in 1991 [14], buckling and bending [15–17], vibrational [18–20], and electronic and optical properties [21–25] of CNTs have been extensively studied in both theoretical and experimental aspects. Because of their unique hollow structure, CNTs may be used for channeling and steering charged particles (e.g., ions [26] and electrons [27]), akin to crystal channeling. Thus, CNTs offer several advantages over natural crystals when it comes to channeling and steering charged particles, such as wider channels in two dimensions and longer dechanneling lengths [28, 29], becoming a robust alternative for TV/m acceleration due to their exceptional electronic properties, greater flexibility, and thermo-mechanical strength. Consequently, carbon nanostructures (CNTs or even graphene layers) are currently being studied for wakefield acceleration [30–34].

Wakefields in CNTs can arise due to the collective oscillation of the free electron gas confined to the surfaces of the nanotubes, which is triggered by the driving bunch. Therefore, the CNT surface can be understood as a plasma composed of free carbon ions and free electrons, whose dynamics is highly susceptible to external electromagnetic fields. In particular, this collective oscillation of electrons is called plasmons because of their similarities with plasmas. On the one hand, plasmons can be theoretically studied by solving the Maxwell's equations in a medium characterized by the electric permittivity. In this sense, several models have been employed, for example, a dielectric theory [35], kinetic models [36, 37], and hydrodynamic models [38–40]. On the other hand, plasmon excitations can also be described by particle simulations, which take into account the motion of the particles. In this context, particle-in-cell (PIC) codes have emerged as a potent instrument to simulate these excitations, although with some limitations [41].

The motivation of the present work is to compare the excited wakefields predicted by the linearized hydrodynamic model [31] with PIC simulations performed with Fourier-Bessel PIC (FBPIC), analyzing the commonalities and discrepancies between both approximations.

This chapter is organized as follows. Section 2 describes the capabilities and limitations of PIC codes, mentioning different recent studies of carbon nanostructures that have been made using such simulations. Section 3 reviews the linearized hydrodynamic, providing general expressions for the longitudinal wakefield excited by the interaction of a charged particle that is traveling paraxially along a CNT. In Section 4, we describe the hollow plasma channel that we consider for modeling the plasmonic excitations in a CNT. Then, we compare the results obtained from the simulations with the hydrodynamic model in Section 5, discussing the similarities and limitations in Section 6. Finally, a summary of the main findings of this study is presented in Section 7.

2. PIC codes

PIC simulations are primarily designed for modeling the behavior of plasmas, where the focus is on the self-consistent dynamics of charged particles and electromagnetic fields. In PIC simulations, the medium is usually modeled as a free electron gas and a neutralizing ionic background. However, most modern PIC codes now incorporate some form of ionization model, such as the Ammosov-Delone-Krainov (ADK) model [42], which allows for the simulation of ionizable atoms. This addition enables a more dynamic and realistic representation of the medium, particularly in scenarios where ionization processes are significant, such as in high-intensity laser-plasma interactions [43]. In these simulations, the electrons are initially randomly distributed according to the density. Then, in each temporal step, the electromagnetic fields (calculated by solving the Maxwell's equations) are used to update the position of each electron, solving the Newton-Lorentz equation. It is worth mentioning that the movement of the electrons produces a local current density, which will affect the electromagnetic fields calculated using Maxwell's equations in the next temporal step. Thus, PIC codes are capable of obtaining the position of each electron as a function of time. PIC simulations can be very time consuming, and for this reason, macroparticles (representing many electrons or positive ions) are normally used. As far as we know, traditional PIC methods are not well-suited for incorporating solid-state effects, such as interactions with the lattice or inter-band transitions, and others are normally neglected due to very time consuming, such as collisions [41]. Nevertheless, PIC codes are especially effective for solving problems that are extremely rapid ($\sim$ sub-fs) and occur at small scales ($\sim$ nm) with a large assembly of charged particles. Consequently, they can be used to study the interaction of laser and beams with plasmas in the context of ultra-high-gradient particle acceleration and plasmon excitation.

Several PIC codes, for example, EPOCH, FBPIC, OSIRIS, PIConGPU, SLIPs, Smilei, and WarpX, have been used in the last decade to simulate laser wakefield acceleration (LWFA) and plasma wakefield acceleration (PWFA) in carbon nanostructures. In the following subsections, we will briefly review these codes and some recent studies conducted using them.

2.1 EPOCH

EPOCH [44] is an open-source PIC code capable to simulate laser-plasma interactions. As with many PIC codes, EPOCH utilizes a staggered Yee grid to resolve the fields and employs a Boris-type pusher [45, 46] to simulate the particle dynamics. Zhang *et al.* [47] performed two-dimensional simulations with EPOCH, showing that a laser propagating inside a nanotube can excite gradients in the order of TV/cm and the emission of high-energy photons in the order of 10–100 MeV. Furthermore, Sangwan *et al.* [48] studied the interaction of a 10 PW laser incident on a fully ionized planar target of carbon. It was shown that carbon ions can be accelerated to energies $\sim$GeV for a target thickness $\sim$ 120 nm, demonstrating that this setup can be used to obtain C^{6+} ions for hadrontherapy treatments.

2.2 FBPIC

Fourier-Bessel PIC (FBPIC) [49] is a code whose solver uses 2D radial grids to calculate azimuthal modes within cylindrical hollow plasma channels. Consequently,

this code allows us to reduce the high computational cost in geometries with cylindrical symmetry compared to 3D PIC codes.

FBPIC has been used to simulate CNTs and bundles of CNTs, modeled as hollow cylindrical channels composed of a pre-ionized cold plasma of two species (electrons and carbon ions). In particular, Bonatto *et al.* [30] have studied the wakefields excited by an external beam traveling along carbon nanostructures, obtaining their dependence on the tube aperture and the wall thickness.

2.3 OSIRIS

OSIRIS [50] is a massively parallel and fully relativistic open-source PIC code for modeling plasma-based accelerators. The PIC algorithm can take into account ionization, classical radiation damping, and quantum electrodynamics (QED) effects. Furthermore, this code implements different geometries (1D, 2D, and 3D) and quasi-3D with azimuthal expansion for cylindrical problems. The OSIRIS code has been employed to study ion acceleration in the radiation pressure regime with 100 TW ultrashort (< 50 fs) pulse lasers interacting with nanometer-scale carbon targets [51].

2.4 PIConGPU

PIConGPU [52] is a computational code designed for laser-plasma simulations that permits the free movement of both electrons and carbon ions. This code is capable to enhance performance proportionally with the number of graphics cards provided. Additionally, it offers a comprehensive array of technical functionalities, including the initialization of macroparticles, various ionization processes, and field-solving techniques, among others. Sharma and Kamperidis [53] used the PIConGPU code to study the interaction of ultrashort, ultra-intense (2 PW, 20 fs) laser pulses with near-critical-density partially ionized plasmas (hydrogen and carbon species), demonstrating the creation of high-energy monochromatic proton micro-bunches of high quality. More recently, Bontoiu *et al.* [34] have utilized this code to simulate electron laser-driven acceleration in ionized graphene layers, revealing a new collective and self-injection mechanism (which was called *catapult acceleration*) based on edge plasma oscillations where gradients of several TV/m can be obtained.

2.5 SLIPs

The spin-resolved laser interaction with plasma simulation code (SLIPs) is capable of performing spin-resolved quantum electrodynamic PIC simulations in laser-matter interactions [54, 55]. In particular, its Monte-Carlo algorithm implements nonlinear Compton scattering and the nonlinear Breit-Wheeler process in the local constant field approximation, vacuum birefringence processes, spin dynamics, and high-energy bremsstrahlung.

Dou *et al.* [56] have recently employed the SLIPs code to investigate the dynamics of positrons in a novel polarized positron acceleration method that combines transition radiation along with electrostatic fields to attain ultra-high gradients. In this method, an ultrarelativistic high-density electron beam traverses any aperture of multi-layer microhole array carbon films, ionizing the film around the aperture that induces a plasma return current. Then, this current produces a net charge accumulation on the film surface, which excites transverse and longitudinal electrostatic fields within and behind the hole that can be utilized to accelerate witness particles.

2.6 Smilei

Smilei [57] is an open-source, highly parallel code that includes additional modules to take into account field ionization and collisions in plasmas. Heppe and Kumar [58] have employed Smilei to demonstrate that laser energy can be efficiently converted into high-energy, brilliant photon beams (~ 300 MeV, $\gtrsim 10^{20}\,\mathrm{s}^{-1}\,\mathrm{mm}^{-2}\mathrm{mrad}^{-2}(0.1\%\mathrm{BW})^{-1}$) in carbon plasmas. In 2024, on the one hand, Azamoum *et al.* [59] have shown that nanometer-thin diamond-like carbon foils may experience a transition from solid to plasma during the laser rising edge employing one-dimensional Smilei simulations; and, on the other hand, Pan *et al.* [60] have demonstrated that electrons can be accelerated through direct laser acceleration in a near-critical density plasma channel composed of carbon nanotube foams.

2.7 WarpX

WarpX is probably the most complete PIC code available today, as it includes the main capabilities of other codes, while also offering dynamic load balancing for CPUs and GPUs, as well as groundbreaking mesh refinement capabilities [61]. Maffini *et al.* [62] have employed WarpX to study laser-driven particle acceleration in a completely ionized homogeneous carbon foam attached to a completely ionized aluminum foil with a 0.05-μm-thick ionized hydrogen layer added on the rear surface of the substrate to simulate contaminants. They demonstrated that MeV protons could be used to conduct particle-induced X-ray emission with comparable performances to conventional sources.

3. Linearized hydrodynamic model

In this work, the excitations caused by a single-charged particle Q on the surface of a CNT are modeled using the linearized hydrodynamic model [31, 40]. This approach conceptualizes a single-walled CNT as a cylinder that is both infinitesimally thin and infinitely long, with a radius a. The delocalized electrons of carbon ions form a two-dimensional Fermi gas (i.e., a free electron gas) initially uniformly distributed (with the surface density n_0) over the CNT surface. Thus, the scenario under consideration involves a point charge moving at a uniform velocity v along the axis of the CNT (the z-axis), as illustrated in **Figure 1**. The position of the driver charge over time t is represented in cylindrical coordinates as $\mathbf{r}_0(t) = (r_0, \varphi_0, vt)$ if we assume that it does not lose energy because of the interaction with the surrounding medium. As a result, the electron gas experiences a perturbation, which is characterized by a velocity field $\mathbf{u}(\mathbf{r_a}, t)$ and a surface density $n(\mathbf{r_a}, t) = n_0 + n_1(\mathbf{r_a}, t)$, where $n_1(\mathbf{r_a}, t)$ is the perturbed density per unit area. Here, $\mathbf{r_a} = (a, \varphi, z)$ specifies the cylindrical coordinates of the CNT surface. In this theory, it is assumed that the electron gas motion is restricted to the CNT surface (i.e., the radial component of $\mathbf{u}$ is zero), and both quantities $\mathbf{u}$ and n_1 are considered to be small perturbations. In the study of wakefield dynamics, it is acceptable to overlook the movement of ions because their motion occurs on a time scale that is significantly slower than the motion of electrons [63, 64]. This is due to the fact that carbon ions have a much larger mass than electrons, resulting in a significantly slower response time.

(a)

(b)
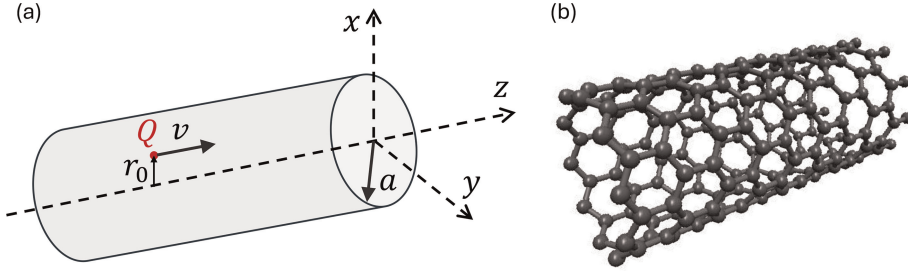
Figure 1.
(a) Schematic of a charge Q moving parallel to the z-axis inside a tube. (b) Schematic of the hexagonal lattice of a CNT.

In this model, the electronic excitations on the CNT wall are characterized by (i) the continuity equation

$$\frac{\partial n_1(\mathbf{r_a}, t)}{\partial t} + n_0 \nabla_\parallel \cdot \mathbf{u}(\mathbf{r_a}, t) = 0, \tag{1}$$

(ii) the Poisson's equation

$$\nabla^2 \Phi(\mathbf{r}, t) = \frac{1}{\varepsilon_0} \left[e n_1(\mathbf{r_a}, t)\delta(r - a) - Q\delta(\mathbf{r} - \mathbf{r}_0) \right], \tag{2}$$

and (iii) the momentum-balance equation

$$\frac{\partial \mathbf{u}(\mathbf{r_a}, t)}{\partial t} = \frac{e}{m_e} \nabla_\parallel \Phi(\mathbf{r_a}, t) - \frac{\alpha}{n_0} \nabla_\parallel n_1(\mathbf{r}, t) + \frac{\beta}{n_0} \nabla_\parallel \left[\nabla_\parallel^2 n_1(\mathbf{r_a}, t) \right] - \gamma \mathbf{u}(\mathbf{r_a}, t). \tag{3}$$

where we have kept terms up to the first order in $\mathbf{u}(\mathbf{r_a}, t)$ and $n_1(\mathbf{r_a}, t)$. In the previous equations, Φ is the electric scalar potential, e is the elementary charge, m_e is the electron mass, ε_0 is the vacuum electric permittivity, δ is the Dirac-delta function, $\nabla = \hat{\mathbf{r}}\frac{\partial}{\partial r} + \hat{\boldsymbol{\varphi}}\frac{1}{r}\frac{\partial}{\partial \varphi} + \hat{\mathbf{z}}\frac{\partial}{\partial z}$ is the nabla operator in cylindrical coordinates, and $\nabla_\parallel = \hat{\boldsymbol{\varphi}}\frac{1}{a}\frac{\partial}{\partial \varphi} + \hat{\mathbf{z}}\frac{\partial}{\partial z}$ only differentiates tangentially to the tube surface. Eq. (3) illustrates the sum of four different elements. The initial term on the right-hand side denotes the force acting upon electrons at the nanotube's surface due to the tangential component of the electric field. The second term accounts for the possible interaction with acoustic modes, establishing the parameter $\alpha = v_F^2/2$ with $v_F = \hbar(2\pi n_0)^{1/2}/m_e$ ($\hbar$ is the reduced Planck constant), representing the Fermi velocity in the 2D electron gas. The third term introduces a quantum correction, which details the single-electron excitations within the electron gas, defining the parameter $\beta = \frac{1}{4}\left(\frac{\hbar}{m_e}\right)^2$. The final term describes a damping force acting on electrons due to their scattering with the ionic-lattice background, denoted by the frictional parameter γ.

The electric potential satisfies the boundary conditions: (i) It vanishes at $r \to \infty$ and (ii) is finite at the origin $r = 0$. Thus, the electric potential can be expanded employing a Fourier-Bessel expansion, that is, using the modified Bessel functions $I_m(x)$ and $K_m(x)$ of integer order m. We will denote the total electric potential inside the nanotube ($r < a$) as Φ_{in} and the total electric potential outside the nanotube ($r > a$) as Φ_{out}. The electric potential inside the nanotube can be expressed as $\Phi_{in} = \Phi_0 + \Phi_{ind}$

with the Coulomb potential Φ_0 generated by the driving charge and the induced potential Φ_{ind} produced by the perturbation of the electron fluid on the CNT surface. The Fourier-Bessel expansion of these magnitudes at a general point $\mathbf{r} = (r, \varphi, z)$ is given by:

$$\Phi_0(\mathbf{r}, t) = \frac{1}{4\pi\varepsilon_0} \frac{Q}{\|\mathbf{r} - \mathbf{r_0}\|} = \frac{Q}{4\pi^2\varepsilon_0} \sum_{m=-\infty}^{+\infty} \int_{-\infty}^{+\infty} dk$$
$$e^{ik\zeta + im(\varphi - \varphi_0)} I_m(|k|r_{\min}) K_m(|k|r_{\max}), \tag{4}$$

$$\Phi_{ind}(\mathbf{r}, t) = \frac{Q}{4\pi^2\varepsilon_0} \sum_{m=-\infty}^{+\infty} \int_{-\infty}^{+\infty} dk\, e^{ik\zeta + im(\varphi - \varphi_0)} I_m(|k|r_0) I_m(|k|r) A_m(k), \tag{5}$$

$$\Phi_{out}(\mathbf{r}, t) = \frac{Q}{4\pi^2\varepsilon_0} \sum_{m=-\infty}^{+\infty} \int_{-\infty}^{+\infty} dk\, e^{ik\zeta + im(\varphi - \varphi_0)} I_m(|k|r_0) K_m(|k|r) B_m(k), \tag{6}$$

where k is the wavenumber, $\zeta = z - vt$ is a comoving coordinate and $r_{\min} = \min(r, r_0)$, $r_{\max} = \max(r, r_0)$. Imposing the boundary conditions: (i) continuity of the electric potential at the nanotube surface

$$\Phi_{in}(\mathbf{r_a}, t) = \Phi_{out}(\mathbf{r_a}, t), \tag{7}$$

and (ii) discontinuity of the radial component of the electric field due to perturbed density n_1 of the electron fluid

$$\left. \frac{\partial \Phi_{out}(\mathbf{r}, t)}{\partial r} \right|_{r=a} - \left. \frac{\partial \Phi_{in}(\mathbf{r}, t)}{\partial r} \right|_{r=a} = \frac{en_1(\mathbf{r_a}, t)}{\varepsilon_0}, \tag{8}$$

the coefficients $A_m(k)$ and $B_m(k)$ can be easily calculated, obtaining

$$A_m(k) = \frac{\Omega_p^2 a^2 (k^2 + m^2/a^2) K_m^2(|k|a)}{kv(kv + i\gamma) - \omega_m^2(k)}, \tag{9}$$

$$B_m(k) = \frac{kv(kv + i\gamma) - \alpha(k^2 + m^2/a^2) - \beta(k^2 + m^2/a^2)^2}{kv(kv + i\gamma) - \omega_m^2(k)}, \tag{10}$$

where $\Omega_p = \sqrt{\frac{e^2 n_0}{\varepsilon_0 m_e a}}$ is the two-dimensional plasma frequency and $\omega_m(k)$ the dispersion relations:

$$\omega_m^2(k) = \alpha\left(k^2 + \frac{m^2}{a^2}\right) + \beta\left(k^2 + \frac{m^2}{a^2}\right)^2 + \Omega_p^2 a^2\left(k^2 + \frac{m^2}{a^2}\right) K_m(|k|a) I_m(|k|a). \tag{11}$$

The induced longitudinal electric wakefield inside the tube is given by

$$W_{z,\text{ind}} = -\frac{\partial \Phi_{\text{ind}}}{\partial z} = \frac{Q}{4\pi^2\varepsilon_0} \sum_{m=-\infty}^{+\infty} \int_{-\infty}^{+\infty} dk\, k e^{im(\varphi - \varphi_0)} I_m(|k|r_0) I_m(|k|r) \times$$
$$[\text{Re}[A_m(k)] \sin(k\zeta) + \text{Im}[A_m(k)] \cos(k\zeta)] = W_{z,\text{Re}} + W_{z,\text{Im}}, \tag{12}$$

which has been separated into two different terms which come from the real and imaginary parts of $A_m(k)$, respectively. To minimize computational time and avoid

artificial numerical errors, a cutoff for large wavenumbers k has to be implemented in the numerical integration. Nevertheless, when the frictional parameter is negligible ($\gamma \rightarrow 0^+$), the term $W_{z,\text{Im}}$ can be analytically integrated (see Appendix B of [31]), obtaining

$$W_{z,\text{Im}}(\gamma \rightarrow 0^+) = \frac{-Q}{2\pi\varepsilon_0} \sum_{m=-\infty}^{+\infty} e^{im(\varphi-\varphi_0)} k_m I_m(k_m r_0) I_m(k_m r)$$

$$\times \Omega_p^2 a^2 \left(k_m^2 + \frac{m^2}{a^2}\right) K_m^2(k_m a) \left|\frac{\partial Z_m}{\partial k}\right|_{k=k_m}^{-1} \cos(k_m \zeta), \tag{13}$$

where k_m are the positive roots of $Z_m(k) = (kv)^2 - \omega_m^2(k)$. Furthermore, it is satisfied that $W_{z,\text{Re}} \approx W_{z,\text{Im}}$ [31]. Thus, the longitudinal wakefield can be approximated by:

$$W_z(\mathbf{r}, t) \approx \frac{-Q}{\pi\varepsilon_0} \sum_{m=-\infty}^{+\infty} e^{im(\varphi-\varphi_0)} k_m I_m(k_m r_0) I_m(k_m r)$$

$$\times \Omega_p^2 a^2 \left(k_m^2 + \frac{m^2}{a^2}\right) K_m^2(k_m a) \left|\frac{\partial Z_m}{\partial k}\right|_{k=k_m}^{-1} \cos(k_m \zeta). \tag{14}$$

In particular, if the charged particle travels on the z-axis (i.e., $r_0 = 0$), Eq. (14) can be simplified because the only non-vanishing mode is $m = 0$:

$$W_z \approx W_z^{max} \cos(k_0 \zeta), \tag{15}$$

$$W_z^{max} = -\frac{Q}{\pi\varepsilon_0} k_0^3 I_0(k_0 r_0) I_0(k_0 r) \Omega_p^2 a^2 K_0^2(k_0 a) \left|\frac{\partial Z_0}{\partial k}\right|_{k=k_0}^{-1}. \tag{16}$$

It is worth noting that Eq. (16) gives the amplitude of the excited longitudinal wakefield.

4. PIC simulations

Carbon nanotubes can be modeled as hollow plasma tubes consisting of layers filled with a uniformly distributed, pre-ionized cold plasma of carbon ions and electrons. We will define a hollow plasma channel model with an inner radius r_{in} and wall thickness w_t with a volumetric density $n_V = 10^{28}\,\text{m}^{-3}$ of free electrons within this region, as shown in **Figure 2**. Because of the high computational cost of 3D PIC simulations and the cylindrical symmetry of the geometry, the FBPIC code is chosen to perform the simulations. We will consider a beam driver with a bi-Gaussian distribution

$$n_b(\zeta, r) = n_b e^{-\zeta^2/(2\sigma_\zeta^2)} e^{-r^2/(2\sigma_r^2)}, \tag{17}$$

where $n_b = (Q_b/e)/\left[(2\pi)^{3/2} \sigma_\zeta \sigma_r^2\right]$ is the peak beam density, $Q_b = -44$ fC is the beam charge, and σ_ζ and σ_r are the beam longitudinal and radial root mean square (RMS) sizes, respectively. It is worth mentioning that, for the sake of comparison, we choose $\sigma_\zeta = \sigma_r = 3.33$ nm $\ll r_{\text{in}}$ to ensure that the beam driver can be approximated by
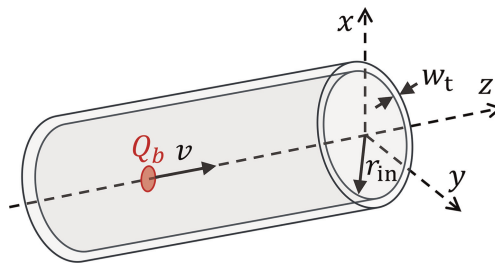
Figure 2.
(a) Scheme considered for PIC simulations: a bi-Gaussian beam driver with charge Q_b moving along the z-axis inside a hollow plasma channel with inner radius r_{in}, wall thickness w_t, and uniform volumetric density n_V.

a point-like charge as in the hydrodynamic model. To minimize changes in the beam distribution along the propagation, all PIC simulations utilized a high-energy beam of 1 GeV (Gaussian distribution, with a standard deviation of 0.005 GeV). The simulation domain was longitudinally set to approximately ∼920 nm, accommodating around 2 to 3 complete wakefield oscillations in the wake of the driver. The maximum radius was defined as the sum of the internal radius (r_{in}), wall thickness (w_t), plus an additional empty region of half of the plasma wavelength ($0.5\lambda_p$) to allow observations of potential oscillations on the external face of the CNT wall. The spatial resolution in z and r coordinates was set to 1/15th of σ_ζ and σ_r, respectively, with a total of 20 particles per cell (8 along z, 8 along r, and 4 along the azimuthal angle θ).

5. Results

The main difference between the PIC simulations and the hydrodynamic model is the definition of a 3D region with free electrons compared to the infinitesimally thin cylindrical surface which is assumed in the hydrodynamic model. Consequently, to compare the results obtained from the simulations and the hydrodynamic model (Eq. (16)), we have to relate the volumetric and surface densities, that is, n_V and n_0. Thus, we will assume that the number of free electrons within the cylindrical surface of radius $a = r_{in}$ is equal to the number of free electrons in the wall thickness w_t. This relation is given by the expression:

$$n_0 = \frac{n_V w_t}{2 r_{in}} (2 r_{in} + w_t).\tag{18}$$

Figure 3 shows the amplitude of the longitudinal wakefield as a function of the CNT radius $a = r_{in}$ for different wall thicknesses. It can be observed that there is a good qualitative agreement between the PIC simulations and the hydrodynamic model.

However, the results obtained with the PIC simulations are lower than the wakefields obtained with the hydrodynamic model for small values of the CNT radius, in particular, for larger wall thicknesses. This behavior is produced because not all free electrons of the wall thickness excite the wakefield effectively; that is, the electrons that are closer to the inner radius have a stronger contribution than the external electrons. For this reason, it seems more reasonable to consider an effective density or an effective wall thickness. In the effective density approach, we consider that the surface density of the linearized hydrodynamic model is given by
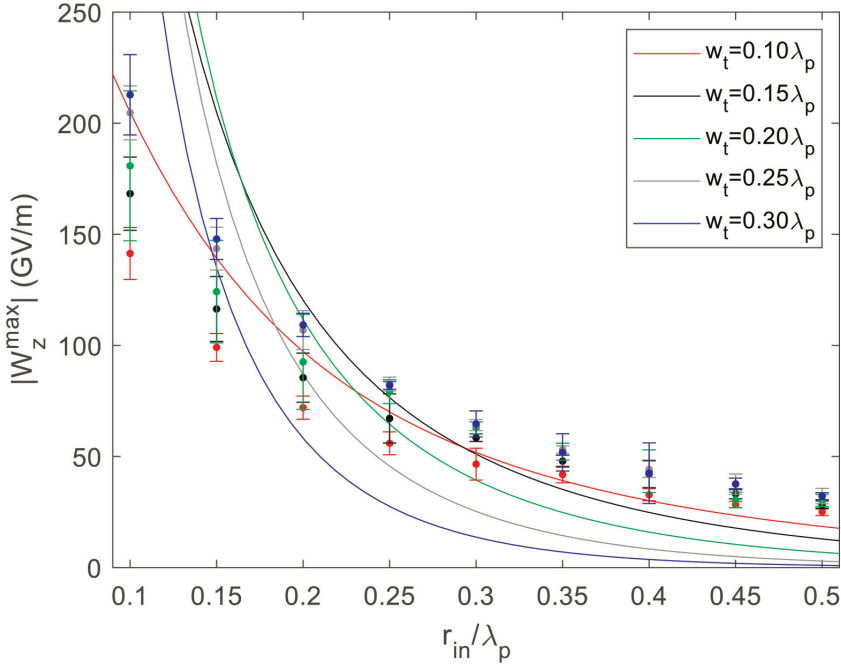
Figure 3.
Amplitude of the longitudinal wakefield on the z-axis (excited by a driver traveling on the axis) as a function of the CNT radius for different wall thicknesses. Solid lines indicate the linearized hydrodynamic model, and the points display results from the PIC simulations. Error bars are estimated from the simulations for different propagation times. The parameters used are: $Q = Q_b = -44\,fC$, $n_V = 10^{28}\ m^{-3}$ and $v \to c$. The lengths are expressed in units of the plasma wavelength $\lambda_p = 2\pi c/\omega_p$, where $\omega_p = \sqrt{e^2 n_V/(m_e \varepsilon_o)}$ is the plasma frequency.

$$n_0 = \kappa \frac{n_V w_t}{2 r_{in}} (2 r_{in} + w_t), \tag{19}$$

which is Eq. (18), but introducing the parameter $\kappa \in (0, 1]$ to take into account the effectiveness of the electrons. In the effective wall thickness approach, the surface density is given by

$$n_0 = \frac{n_V w_t^{eff}}{2 r_{in}} (2 r_{in} + w_t^{eff}), \tag{20}$$

where the effective wall thickness $w_t^{eff} \leq w_t$ is introduced compared to Eq. (18). Thus, **Figures 4** and **5** depict the amplitude of the excited longitudinal wakefield employing the effective density and effective wall thickness approaches, respectively, using the numerical values collected in **Table 1** and plotted in **Figure 6**. We can see a better agreement between these approximations and the PIC simulations. As it is intuitively expected, the parameter κ decreases as a function of the wall thickness, while the effective wall thickness w_t^{eff} increases.

6. Discussion

The discrepancies observed between the hydrodynamic model and the PIC simulations can be attributed to the distinctions in both approaches. In the hydrodynamic
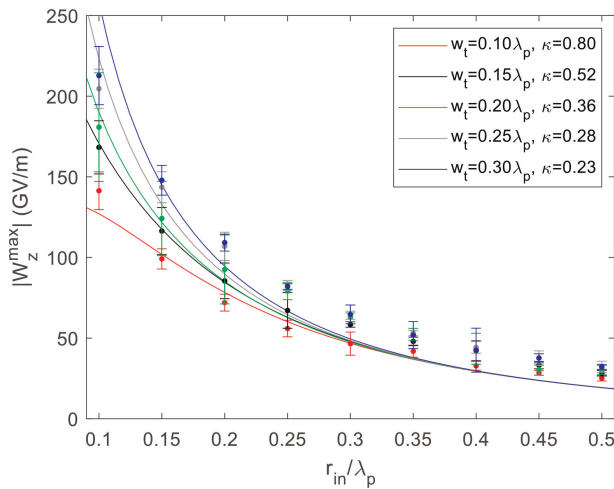
Figure 4.
*Amplitude of the longitudinal wakefield on the z-axis (excited by a driver traveling on the axis) as a function of the CNT radius for different wall thicknesses. Solid lines indicate the linearized hydrodynamic model using the effective density approach with the values shown in **Table 1**, and the points display results from the PIC simulations. Error bars are estimated from the simulations for different propagation times. We use the same parameters as in **Figure 3**: $Q = Q_b = -44\,fC$, $n_V = 10^{28}\ m^{-3}$ and $v \to c$.*
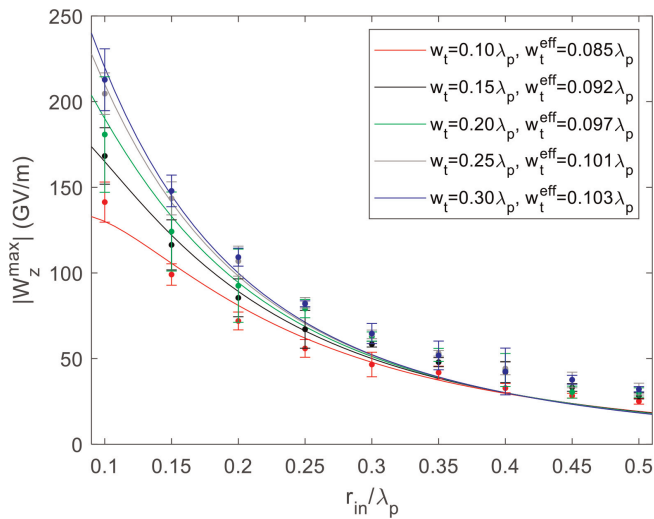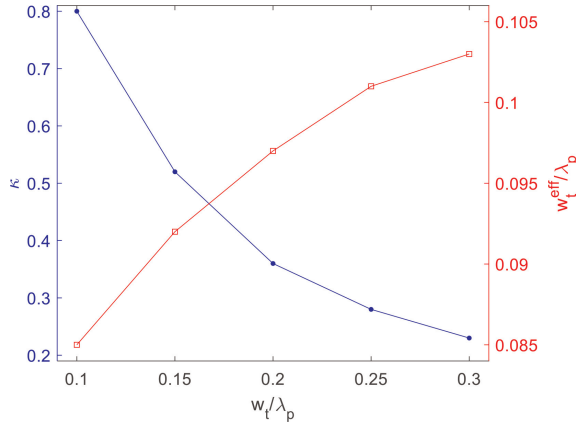

Figure 5.
*Amplitude of the longitudinal wakefield on the z-axis (excited by a driver traveling on the axis) as a function of the CNT radius for different wall thicknesses. Solid lines indicate the linearized hydrodynamic model using the effective wall thickness approach with the values shown in **Table 1** and the points display results from the PIC simulations. Error bars are estimated from the simulations for different propagation times. We use the same parameters as in **Figure 3**: $Q = Q_b = -44\,fC$, $n_V = 10^{28}\ m^{-3}$ and $v \to c$.*

model, the driver is a point-like particle, with dynamics decoupled from the surrounding medium. Once defined, its properties (charge, radial position, and longitudinal velocity) remain unchanged. In contrast, in PIC simulations, the driver is modeled as a bi-Gaussian beam consisting of a large number of particles distributed within a finite volume. Moreover, since PIC simulations self-consistently resolve the

Wall thickness: w_t	Effective density approach: κ	Effective wall thickness approach: w_t^{eff}
$0.10\lambda_p$	0.80	$0.085\lambda_p$
$0.15\lambda_p$	0.52	$0.092\lambda_p$
$0.20\lambda_p$	0.36	$0.097\lambda_p$
$0.25\lambda_p$	0.28	$0.101\lambda_p$
$0.30\lambda_p$	0.23	$0.103\lambda_p$

Table 1.
Summary of the numerical values of the parameters κ and w_t^{eff} employed in the effective density and effective wall thickness approaches.

Figure 6.
Parameter κ (defined in Eq. (19)) and effective wall thickness w_t^{eff} as a function of the wall thickness w_t.

dynamics of all charged particles, the driver and the surrounding medium are both affected by mutual interactions and self-interactions.

For a proper comparison with the hydrodynamic model, the beam size in a PIC simulation must be smaller than the tube aperture. This requires a higher spatial resolution, which in turn increases the simulation time. Additionally, it results in a high-density beam, making it susceptible to stronger space-charge effects. These effects can alter the beam distribution and modify the properties of the driven wakefields. For highly relativistic beams ($v \sim c$), the driver evolution along short propagation distances is negligible. However, lower-energy beams are susceptible to significant changes in their spatial distribution and velocity reduction due to energy loss caused by interactions with their self-driven fields.

Hence, while PIC simulations with highly relativistic beams behave more similar to the hydrodynamic model, the latter was developed within a nonrelativistic framework. This discrepancy introduces additional challenges in establishing a direct comparison, but there are strategies to mitigate these issues. For example, one could artificially increase the mass of the beam particles and eliminate the energy spread.

Another source of discrepancy arises from the absence of solid-state properties in PIC simulations. These characteristics, modeled in the hydrodynamic model using

parameters α, β, and γ, describe the collective behavior of electrons within CNTs. In CNTs, electron motion along the surface is facilitated, allowing for easier longitudinal movement while remaining constrained. However, in PIC simulations, electrons can move equally in any direction. This is because there are no mechanisms to specifically constrain them to the CNT surface. Even if collisions or interactions are modeled using algorithms like Monte-Carlo Collisions (MCC) or Fokker-Planck operators, conventional PIC solvers cannot differentiate between radial and longitudinal movements, nor do they restrict electron motion to the CNT surface. In contrast, the hydrodynamic model incorporates these interactions and restrictions through the friction parameter γ.

Furthermore, we are contrasting a three-dimensional region populated with free electrons (initially a thick cylinder with inner radius r_{in} and wall thickness w_t) in the PIC simulations against a two-dimensional cylindrical surface with radius a in the hydrodynamic model. While the electrons and carbon ions that make up the carbon nanotube are free to move in three dimensions in the simulations, in the hydrodynamic model they are considered to be restricted to the surface.

Thus, taking into account the differences between both approaches, the agreement between the results is satisfactory and consequently, the linearized hydrodynamic model (with the effective approaches) becomes an interesting tool to estimate the excited longitudinal wakefields in CNTs, avoiding time-consuming PIC simulations.

7. Conclusions and outlook

In this chapter, we have described the main characteristics and limitations of PIC codes. Furthermore, we have reviewed some works that have analyzed the wakefield excitation in carbon nanostructures with different PIC codes. Also, the wakefield excited by a driving charge moving through a carbon nanotube has been determined making use of the linearized hydrodynamic model and compared with PIC simulations. The results demonstrate a relatively good agreement of the wakefield amplitude when comparing the theoretical model with simulations. The quantitative agreement is improved if we consider an effective density or an effective wall thickness to take into account an average response of the electrons within the wall thickness in the PIC simulations. We have also discussed the main similarities and differences between the theoretical model and PIC simulations. Thus, it has been demonstrated that the hydrodynamic model may offer a fast method for estimating the excited wakefield in hollow plasmas with thin walls, becoming an alternative for bypassing the need for time-consuming PIC simulations.

Acknowledgements

Abbreviations

ADK	Ammosov-Delone-Krainov
CNT	carbon nanotube

EPOCH   extendable particle-in-cell open collaboration
FBPIC   Fourier-Bessel particle-in-cell
LWFA   laser wakefield acceleration
MCC   Monte Carlo Collisions
PIC   particle-in-cell
PIConGPU   particle-in-cell on graphics processing unit
PWFA   plasma wakefield acceleration
QED   quantum electrodynamics
RF   radio frequency
RMS   root mean square
SLIPs   spin-resolved laser interaction with plasma simulation

Author details

Pablo Martín-Luna[1*], Alexandre Bonatto[2], Cristian Bontoiu[3,4], Guoxing Xia[4,5] and Javier Resta-López[6*]

1 Instituto de Física Corpuscular (IFIC), Universitat de València - Consejo Superior de Investigaciones Científicas, Paterna, Spain

2 Graduate Program in Information Technology and Healthcare Management, and the Beam Physics Group, Federal University of Health Sciences of Porto Alegre, Porto Alegre, RS, Brazil

3 Department of Physics, The University of Liverpool, Liverpool, United Kingdom

4 The Cockcroft Institute, Sci-Tech Daresbury, Warrington, United Kingdom

5 Department of Physics and Astronomy, The University of Manchester, Manchester, United Kingdom

6 Instituto de Ciencia de los Materiales (ICMUV), Universitat de València, Valencia, Spain

*Address all correspondence to: pablo.martin@uv.es and javier2.resta@uv.es

IntechOpen

References

[1] Abe T, Kageyama T, Sakai H, Takeuchi Y, Yoshino K. Breakdown study based on direct in situ observation of inner surfaces of an rf accelerating cavity during a high-gradient test. Physical Review Accelerators and Beams. 2016;**19**:102001. DOI: 10.1103/PhysRevAccelBeams.19.102001

[2] Shao J. Investigations on rf Breakdown Phenomenon in High Gradient Accelerating Structures. Singapore, Singapore: Springer; 2018. DOI: 10.1007/978-981-10-7926-9

[3] Thompson MC, Badakov H, Cook AM, Rosenzweig JB, Tikhoplav R, Travish G, et al. Breakdown limits on gigavolt-per-meter electron-beam-driven wakefields in dielectric structures. Physical Review Letters. 2008;**100**:214801. DOI: 10.1103/PhysRevLett.100.214801

[4] Breuer J, Hommelhoff P. Laser-based acceleration of nonrelativistic electrons at a dielectric structure. Physical Review Letters. 2013;**111**:134803. DOI: 10.1103/PhysRevLett.111.134803

[5] England RJ, Noble RJ, Bane K, Dowell DH, Ng CK, Spencer JE, et al. Dielectric laser accelerators. Reviews of Modern Physics. 2014;**86**:1337-1389. DOI: 10.1103/RevModPhys.86.1337

[6] O'Shea B, Andonian G, Barber S, Fitzmorris K, Hakimi S, Harrison J, et al. Observation of acceleration and deceleration in gigaelectron-volt-per-metre gradient dielectric wakefield accelerators. Nature Communications. 2016;**7**(1):1-7. DOI: 10.1038/ncomms12763

[7] Tajima T, Dawson JM. Laser electron accelerator. Physical Review Letters. 1979;**43**:267-270. DOI: 10.1103/PhysRevLett.43.267

[8] Chen P, Dawson JM, Huff RW, Katsouleas T. Acceleration of electrons by the interaction of a bunched electron beam with a plasma. Physical Review Letters. 1985;**54**:693-696. DOI: 10.1103/PhysRevLett.54.693

[9] Leemans WP, Nagler B, Gonsalves AJ, Tóth C, Nakamura K, Geddes CG, et al. GeV electron beams from a centimetre-scale accelerator. Nature Physics. 2006;**2**(10):696-699. DOI: 10.1038/nphys418

[10] Litos M, Adli E, An W, Clarke C, Clayton C, Corde S, et al. High-efficiency acceleration of an electron beam in a plasma wakefield accelerator. Nature. 2014;**515**(7525):92-95. DOI: 10.1038/nature13882

[11] Tajima T, Cavenago M. Crystal x-ray accelerator. Physical Review Letters. 1987;**59**:1440-1443. DOI: 10.1103/PhysRevLett.59.1440

[12] Chen P, Noble RJ. A solid state accelerator. In: AIP Conf. Proc. Vol. 156. New York: AIP; 1987. pp. 222-227. DOI: 10.1063/1.36458

[13] Chen P, Noble RJ. Crystal channel collider: Ultra-high energy and luminosity in the next century. In: AIP Conf. Proc. Vol. 398. New York: AIP; 1997. pp. 273-285. DOI: 10.1063/1.53055

[14] Iijima S. Helical microtubules of graphitic carbon. Nature. 1991;**354**(6348):56-58. DOI: 10.1038/354056a0

[15] Wong EW, Sheehan PE, Lieber CM. Nanobeam mechanics: Elasticity, strength, and toughness of nanorods and nanotubes. Science. 1997;**277**(5334):1971-1975. DOI: 10.1126/science.277.5334.1971

[16] Salvetat JP, Briggs GAD, Bonard JM, Bacsa RR, Kulik AJ, Stöckli T, et al. Elastic and shear moduli of single-walled carbon nanotube ropes. Physical Review Letters. 1999;**82**:944-947. DOI: 10.1103/ PhysRevLett.82.944

[17] Yakobson BI, Brabec CJ, Bernholc J. Nanomechanics of carbon tubes: Instabilities beyond linear response. Physical Review Letters. 1996;**76**: 2511-2514. DOI: 10.1103/ PhysRevLett.76.2511

[18] Yoon J, Ru CQ, Mioduchowski A. Vibration of an embedded multiwall carbon nanotube. Composites Science and Technology. 2003;**63**(11):1533-1542. DOI: 10.1016/S0266-3538(03)00058-7

[19] Wang CY, Ru CQ, Mioduchowski A. Free vibration of multiwall carbon nanotubes. Journal of Applied Physics. 2005;**97**(11):114323. DOI: 10.1063/ 1.1898445

[20] Ghavanloo E, Fazelzadeh SA. Vibration characteristics of single-walled carbon nanotubes based on an anisotropic elastic shell model including chirality effect. Applied Mathematical Modelling. 2012;**36**(10):4988-5000. DOI: 10.1016/j.apm.2011.12.036

[21] Bursill LA, Stadelmann PA, Peng JL, Prawer S. Surface plasmon observed for carbon nanotubes. Physical Review B. 1994;**49**:2882-2887. DOI: 10.1103/ PhysRevB.49.2882

[22] Lin MF, Chuu DS, Huang CS, Lin YK, Shung KWK. Collective excitations in a single-layer carbon nanotube. Physical Review B. 1996;**53**: 15493-15496. DOI: 10.1103/ PhysRevB.53.15493

[23] Östling D, Tománek D, Rosén A. Electronic structure of single-wall, multiwall, and filled carbon nanotubes.

Physical Review B. 1997;**55**:13980-13988. DOI: 10.1103/PhysRevB.55.13980

[24] Marinopoulos AG, Reining L, Rubio A, Vast N. Optical and loss spectra of carbon nanotubes: Depolarization effects and Intertube interactions. Physical Review Letters. 2003;**91**: 046402. DOI: 10.1103/PhysRevLett. 91.046402

[25] Dmitrović S, Vuković T, Nikolić B, Damnjanović M, Milošević I. Plasmon excitations of single-wall carbon nanotubes. Physical Review B. 2008;**77**: 245415. DOI: 10.1103/PhysRevB.77. 245415

[26] Zhu Z, Zhu D, Lu R, Xu Z, Zhang W, Xia H. The experimental progress in studying of channeling of charged particles along nanostructure. In: Dabagov SB, editor. International Conference on Charged and Neutral Particles Channeling Phenomena, Society of Photo-Optical Instrumentation Engineers (SPIE) Conference Series. Vol. 5974. Bellingham, WA: SPIE; 2006. pp. 382-389. DOI: 10.1117/12.640101

[27] Chai G, Heinrich H, Chow L, Schenkel T. Electron transport through single carbon nanotubes. Applied Physics Letters. 2007;**91**(10):103101. DOI: 10.1063/1.2778551

[28] Biryukov VM, Bellucci S. Nanotube diameter optimal for channeling of high-energy particle beam. Physics Letters B. 2002;**542**(1):111-115. DOI: 10.1016/ S0370-2693(02)02276-1

[29] Bellucci S, Biryukov VM, Cordelli A. Channeling of high-energy particles in a multi-wall nanotube. Physics Letters B. 2005;**608**(1):53-58. DOI: 10.1016/j. physletb.2005.01.003

[30] Bonatto A, Xia G, Apsimon O, Bontoiu C, Kukstas E, Rodin V, et al.

Exploring ultra-high-intensity wakefields in carbon nanotube arrays: An effective plasma-density approach. Physics of Plasmas. 2023;**30**(3):033105. DOI: 10.1063/5.0134960

[31] Martín-Luna P, Bonatto A, Bontoiu C, Xia G, Resta-López J. Excitation of wakefields in carbon nanotubes: A hydrodynamic model approach. New Journal of Physics. 2023; **25**(12):123029. DOI: 10.1088/1367-2630/ad127c

[32] Martín-Luna P, Bonatto A, Bontoiu C, Xia G, Resta-López J. Plasmonic excitations in double-walled carbon nanotubes. Results in Physics. 2024;**60**:107698. DOI: 10.1016/j.rinp.2024.107698

[33] Martín-Luna P, Resta-López J. Excitation of plasmonic wakefields in multi-walled carbon nanotubes: A hydrodynamic approach. In: Kuznetsov DA, editor. Carbon Nanotubes - Recent Advances, Perspectives and Applications. Rijeka: IntechOpen; 2024. DOI: 10.5772/intechopen.114270

[34] Bonţoiu C, Apsimon O, Kukstas E, Rodin V, Yadav M, Welsch C, et al. TeV/m catapult acceleration of electrons in graphene layers. Scientific Reports. 2023; **13**:1330. DOI: 10.1038/s41598-023-28617-w

[35] Wang YN, Mišković ZL. Energy loss of charged particles moving in cylindrical tubules. Physical Review A. 2002;**66**:042904. DOI: 10.1103/PhysRevA.66.042904

[36] Song YH, Zhao D, Wang YN. Kinetic study on self-energy and stopping power of charged particles moving in metallic carbon nanotubes. Physical Review A. 2008;**78**:012901. DOI: 10.1103/PhysRevA.78.012901

[37] Zhang YY, Sun JZ, Song YH, Mišković ZL, Wang YN. Channeling of protons in single-walled carbon nanotubes based on kinetic and molecular-dynamics treatment. Carbon. 2014;**71**:196-205. DOI: 10.1016/j.carbon.2014.01.030

[38] Stöckli T, Bonard JM, Châtelain A, Wang ZL, Stadelmann P. Collective oscillations in a single-wall carbon nanotube excited by fast electrons. Physical Review B. 2001;**64**:115424. DOI: 10.1103/PhysRevB.64.115424

[39] Mowbray DJ, Mišković ZL, Goodman FO, Wang YN. Wake effect in interactions of fast ions with carbon nanotubes. Physics Letters A. 2004; **329**(1):94-99. DOI: 10.1016/j.physleta.2004.06.090

[40] Wang YN, Mišković ZL. Interactions of fast ions with carbon nanotubes: Self-energy and stopping power. Physical Review A. 2004;**69**:022901. DOI: 10.1103/PhysRevA.69.022901

[41] Ding WJ, Lim JZJ, Do HTB, Xiong X, Mahfoud Z, Png CE, et al. Particle simulation of plasmons. Nano. 2020; **9**(10):3303-3313. DOI: 10.1515/nanoph-2020-0067

[42] Ammosov MV, Delone NB, Krainov VP. Tunnel ionization of complex atoms and of atomic ions in an alternating electromagnetic field. Soviet Journal of Experimental and Theoretical Physics. 1986;**64**(6):1191. DOI: 10.1117/12.938695

[43] Chen M, Cormier-Michel E, Geddes CGR, Bruhwiler DL, Yu LL, Esarey E, et al. Numerical modeling of laser tunneling ionization in explicit particle-in-cell codes. Journal of Computational Physics. 2013;**236**:220-228. DOI: 10.1016/j.jcp.2012.11.029

[44] Arber TD, Bennett K, Brady CS, Lawrence-Douglas A, Ramsay MG, Sircombe NJ, et al. Contemporary particle-in-cell approach to laser-plasma modelling. Plasma Physics and Controlled Fusion. 2015;**57**(11):113001. DOI: 10.1088/0741-3335/57/11/113001

[45] Boris JP. Relativistic plasma simulation-optimization of a hybrid code. In: Proc. Fourth Conf. Numerical Simulations of Plasmas. Washington, D. C.: Naval Research Laboratory; 1970. pp. 3-67 Available from: https://apps. dtic.mil/sti/citations/ADA023511

[46] Ripperda B, Bacchini F, Teunissen J, Xia C, Porth O, Sironi L, et al. A comprehensive comparison of relativistic particle integrators. The Astrophysical Journal Supplement Series. 2018;**235**(1):21. DOI: 10.3847/1538-4365/aab114

[47] Zhang X, Tajima T, Farinella D, Shin Y, Mourou G, Wheeler J, et al. Particle-in-cell simulation of x-ray Wakefield acceleration and betatron radiation in nanotubes. Physical Review Accelerators and Beams. 2016;**19**: 101004. DOI: 10.1103/PhysRevAccelBeams.19.101004

[48] Sangwan D, Culfa O, Ridgers CP, Aogaki S, Stutman D, Diaconescu B. Simulations of carbon ion acceleration by 10 PW laser pulses on ELI-NP. Laser and Particle Beams. 2019;**37**(4):346-353. DOI: 10.1017/S0263034619000648

[49] Lehe R, Kirchen M, Andriyash IA, Godfrey BB, Vay JL. A spectral, quasi-cylindrical and dispersion-free particle-in-cell algorithm. Computer Physics Communications. 2016;**203**:66-82. DOI: 10.1016/j.cpc.2016.02.007

[50] Fonseca RA, Silva LO, Tsung FS, Decyk VK, Lu W, Ren C, et al. OSIRIS: A three-dimensional, fully relativistic particle in cell code for Modeling plasma based accelerators. In: PMA S, Hoekstra AG, CJK T, Dongarra JJ, editors. Computational Science — ICCS 2002. Berlin, Heidelberg: Springer Berlin Heidelberg; 2002. pp. 342-351. DOI: 10.1007/3-540-47789-6_36

[51] Dover NP, Najmudin Z. Ion acceleration in the radiation pressure regime with ultrashort pulse lasers. High Energy Density Physics. 2012;**8**(2): 170-174. DOI: 10.1016/j.hedp.2012.02.002

[52] Bussmann M, Burau H, Cowan TE, Debus A, Huebl A, Juckeland G, et al. Radiative signatures of the relativistic kelvin-Helmholtz instability. In: Proceedings of the International Conference on High Performance Computing, Networking, Storage and Analysis. SC'13. Association for Computing Machinery: New York, NY, USA; 2013. DOI: 10.1145/2503210.2504564

[53] Sharma A, Kamperidis C. High energy proton micro-bunches from a laser plasma accelerator. Scientific Reports. 2019;**9**:13840. DOI: 10.1038/s41598-019-50348-0

[54] Wan F, Lv C, Xue K, Dou ZK, Zhao Q, Ababekri M, et al. Simulations of spin/polarization-resolved laser–plasma interactions in the nonlinear QED regime. Matter and Radiation at Extremes. 2023;**8**(6):064002. DOI: 10.1063/5.0163929

[55] Xue K, Sun T, Wei KJ, Li ZP, Zhao Q, Wan F, et al. Generation of high-density high-polarization positrons via single-shot strong laser-foil interaction. Physical Review Letters. 2023;**131**:175101. DOI: 10.1103/PhysRevLett.131.175101

[56] Dou ZK, Lv C, Salamin YI, Zhang N, Wan F, Xu ZF, et al. Compact spin-

polarized positron acceleration in multi-layer microhole array films. ARXIV. 2024. Available from: https://arxiv.org/abs/2405.11186

[57] Derouillat J, Beck A, Pérez F, Vinci T, Chiaramello M, Grassi A, et al. Smilei: A collaborative, open-source, multi-purpose particle-in-cell code for plasma simulation. Computer Physics Communications. 2018;**222**:351-373. DOI: 10.1016/j.cpc.2017.09.024

[58] Heppe C, Kumar N. High brilliance γ-ray generation from the laser interaction in a carbon plasma channel. Frontiers in Physics. 2022:**10**:987830. DOI: 10.3389/fphy.2022.987830

[59] Azamoum Y, Becker GA, Keppler S, Duchateau G, Skupin S, Grech M, et al. Optical probing of ultrafast laser-induced solid-to-overdense-plasma transitions. Light: Science Applications. 2024;**13**:109. DOI: 10.1038/s41377-024-01444-y

[60] Pan Z, Liu J, Wang P, Mei Z, Cao Z, Kong D, et al. Electron acceleration and x-ray generation from near-critical-density carbon nanotube foams driven by moderately relativistic lasers. Physics of Plasmas. 2024;**31**(4):043108. DOI: 10.1063/5.0202843

[61] Fedeli L, Huebl A, Boillod-Cerneux F, Clark T, Gott K, Hillairet C, et al. Pushing the Frontier in the design of laser-based electron accelerators with groundbreaking mesh-refined particle-in-cell simulations on exascale-class supercomputers. In: SC22: International Conference for High Performance Computing, Networking, Storage and Analysis. Dallas, Texas, USA: IEEE; 2022. pp. 1-12. DOI: 10.1109/SC41404.2022.00008

[62] Maffini A, Mirani F, Galbiati M, Ambrogioni K, Gatti F, Galli De

Magistris MS, et al. Towards compact laser-driven accelerators: Exploring the potential of advanced double-layer targets. EPJ Techniques and Instrumentation. 2023;**10**:15. DOI: 10.1140/epjti/s40485-023-00102-8

[63] Hakimi S, Nguyen T, Farinella D, Lau CK, Wang HY, Taborek P, et al. Wakefield in solid state plasma with the ionic lattice force. Physics of Plasmas. 2018;**25**(2):023112. DOI: 10.1063/1.5016445

[64] Hakimi S, Zhang X, Lau C, Taborek P, Dollar F, Tajima T. X-ray laser Wakefield acceleration in a nanotube. International Journal of Modern Physics A. 2019;**34**(34): 1943011. DOI: 10.1142/S0217751X19430115